Chemical Papers
https://doi.org/10.1007/s11696-020-01489-4

ORIGINAL PAPER

Structural, morphological and photoluminescence properties of β-Ag_2MoO_4 doped with Eu^{3+}

Priscila B. Almeida[1] · Ivo M. Pinatti[1] · Regiane C. de Oliveira[2,3] · Mayara M. Teixeira[1] · Clayane C. Santos[1] · Thales R. Machado[1] · Elson Longo[1] · Ieda L. V. Rosa[1]

Received: 8 July 2020 / Accepted: 19 December 2020

Abstract
In this work, we report the investigation on β-$Ag_{(2-3x)}Eu_xMoO_4$ ($x = 0.0$; 0.0025; 0.005; 0.0075, and 0.01 mmol) materials prepared using the coprecipitation method. X-ray diffraction (XRD), Rietveld refinement analysis, and Raman spectroscopy confirmed that all of the synthesized β-$Ag_{(2-3x)}Eu_xMoO_4$ samples were perfectly monophasic, with spinel-like cubic structure. The results obtained in the morphological analysis indicate that the insertion of the Eu^{3+} ion into the β-Ag_2MoO_4 matrix favors the formation of surface defects and suggests that in higher concentrations of dopant the particles become more geometrically defined. The photoluminescence analysis (PL) was performed using two excitation sources: krypton laser and xenon lamp. Through the emission and excitation spectra it was observed that β-Ag_2MoO_4 exhibits broad band in the blue region, and as the concentration of Eu^{3+} increases this emission is gradually suppressed, giving rise to an intense emission with narrow and well-defined lines in the red region, confirming β-Ag_2MoO_4 as a good matrix capable of sensitizing and stabilizing the red emission of the Eu^{3+} ion. In addition, all other characterizations demonstrate that the replacement of Ag^+ by Eu^{3+} ions caused structural, morphological, and optical changes with lattice disturbances in the short, medium, and long ranges.

Keywords Silver molybdate · Europium · Doping · Morphological analysis · Photoluminescence

Introduction

The study of advanced inorganic materials constitutes a multidisciplinary research field, considering the vast potential applications of this class of functional materials. In this scenario, molybdates have occupied a prominent position in the investigation of the structural/optoelectronic behavior of new materials (Lim 2016; Laciste et al. 2017; Guo et al. 2008; Sun et al. 2016). These materials have high chemical stability due to the organization of their atomic arrangements, allowing their application in different systems. In particular, silver molybdate (Ag_2MoO_4) has been used in photocatalysts (Ferreira et al. 2019; Della Rocca et al. 2020; Yang et al. 2017; Warmuth et al. 2020), antimicrobial agents (Oliveira et al. 2017; Fabbro et al. 2016; De Foggi et al. 2020; Tang et al. 2013; Moura et al. 2017), sensors (Pachauri et al. 2020; Kumar et al. 2016), in optoelectronic, and luminescent devices (De Santana et al. 2014; Gouveia et al. 2014).

Ag_2MoO_4 has two phases related to the metastable α-Ag_2MoO_4 and stable β-Ag_2MoO_4. The α-Ag_2MoO_4 usually requires drastic conditions of synthesis, such as high temperatures and pressures, as well as sophisticated equipments. Besides that, during the synthesis, α-Ag_2MoO_4 can be irreversibly transformed to β-Ag_2MoO_4 (Beltrán et al. 2014; Ng and Fan 2015). The β-Ag_2MoO_4 phase consists of Mo^{6+} coordinated to four O^{2-} anions to form the tetrahedral [MoO_4] clusters, and the Ag^+ cations are coordinated to six O^{2-} anions forming octahedral [AgO_6]

Supplementary Information The online version contains supplementary material available at https://doi.org/10.1007/s11696-020-01489-4.

✉ Ieda L. V. Rosa
ilvrosa@ufscar.br

[1] Chemistry Departament, CDMF, Federal University of São Carlos, P. O. Box 676, São Carlos 13565-905, Brazil

[2] Faculty of Engineering of Guaratinguetá, São Paulo State University, UNESP, Guaratinguetá, SP 12516-410, Brazil

[3] Modeling and Molecular Simulations Group, São Paulo State University, UNESP, Bauru, SP 17033-360, Brazil

Published online: 04 January 2021

clusters. The electronic structure shows that these materials present energy gap (E_{gap}) values between 3.2 and 3.4 eV (Moura et al. 2016; Fabbro et al. 2015).

To obtain pure and doped molybdates, different synthetic routes are used by varying parameters such as pH, temperature, and precursors. These materials may exhibit different sizes, morphologies, and properties (Wang et al. 2017; Singh et al. 2012; Jiang et al. 2015). More traditional synthetic methods require complex conditions and do not always guarantee the homogeneity and regularity of the crystals (Pan et al. 2007; Montenegro et al. 2018; Kaddouri et al. 2004). Therefore, to overcome these drawbacks, sustainable methodologies have become an interesting alternative for the development of functional materials (Kianpour et al. 2016; Shahri et al. 2013). The co-precipitation methodology, a widely used technique, avoids these problems and is considered a green experimental procedure, since it uses environmentally friendly solvent (water), low processing temperatures, and is an easily reproducible method. This procedure allows the formation of single-phase crystals with homogeneous sizes and shapes. Furthermore, this method allows the incorporation of different dopants in the crystal lattice to shape and extend the functionality of inorganic materials (Kianpour et al. 2016).

The efficiency of doping in different matrices using rare earths (RE) is a consolidated subject in the literature. The unique optical properties of these elements are known to be associated mainly with transitions 4*f*–4*f* or 5*d*–4*f* transitions due to their electronic configurations (Erwin et al. 2005; Krishna Bharat et al. 2014; Dai 2017). Among RE, europium (Eu) is one of the most studied (Wang et al. 2019). In the trivalent state (Eu^{3+}), this ion presents an electronic configuration $4f^6$, with the innermost orbital electrons protected from the chemical environment by the outermost ones (Binnemans 2009; Tymiński and Grzyb 2017), resulting in fine and well-defined emission lines (Cichos et al. 2016). In general, the intentional insertion of Eu^{3+} results in very marked changes in the PL properties of the host matrix (Erwin et al. 2005; Cichos et al. 2016; Tymiński and Grzyb 2017) especially in the case of molybdates, which are known to be excellent receptors for this ion. Thus, the parameter control of synthesis and doping are resources used to promote changes in the morphological and optical properties of molybdates. The first feature is well exemplified in the study by Songchu et al. (Li et al. 2017), which synthesized strontium and barium molybdates using isopropanol as solvent, varying the concentration of hexadecyl trimethyl ammonium (CTAB) precursor and the pH of the reactional medium. In addition, the use of Eu^{3+} in the β-Ag_2MoO_4 matrix was addressed in the study developed by Gupta et al. (Gupta et al. 2015). In this work, the researchers demonstrate the photoluminescent properties of the studied materials, making a comparison between the pure and Eu^{3+} doped samples with a fixed concentration of 0.01 mmol of Eu^{3+}.

In our study, we describe the synthesis of β-$Ag_{(2-3x)}Eu_xMoO_4$ phosphors by varying the concentrations of Eu^{3+} ($x = 0.0$; 0.0025; 0.005; 0.0075, and 0.01 mmol) to observe whether there is a trend in the photoluminescent behavior and thus understand how these changes affect the characteristic emissions of these materials when they are excited by two different excitation sources, laser and xenon lamp. In the same direction, we investigated structural changes and morphological behavior with the aid of scanning and transmission electron microscopy micrographs, a discussion presented for these structures for the first time. These investigations were carried out using the techniques of X-ray diffraction (XRD) and Rietveld refinement, Raman spectroscopy, scanning electron microscopy (SEM) and transmission electron microscopy (TEM), ultraviolet–visible diffuse reflectance (UV–vis) spectroscopy, and photoluminescence measurements (PL).

Experimental

Synthesis

Firstly, pure β-Ag_2MoO_4 was prepared by dissolving 1.0 mmol of sodium molybdate ($Na_2MoO_4.2H_2O$, Sigma-Aldrich, 99.5%) in 50 mL of deionized water. Separately, 2.0 mmol of silver nitrate ($AgNO_3$, Sigma-Aldrich, 99.99%) was dissolved in 50 mL of deionized water. Both solutions were prepared at 80 °C, under magnetic stirring for 15 min. These solutions were quickly mixed, promoting the instantaneous formation of a solid β-Ag_2MoO_4 precipitate (beige coloration). The precipitate was centrifuged, washed with distilled water several times, and dried in a conventional oven at 60 °C overnight. The β-$Ag_{(2-3x)}Eu_xMoO_4$ ($x = 0.0$; 0.0025; 0.005; 0.0075, and 0.01 mmol) powders, were prepared using the same procedure described above, but the solutions containing different amounts of Eu^{3+} ions were added to the $AgNO_3$ solutions. The $Eu(NO_3)_3$ solution was obtained by dissolving europium oxide (Eu_2O_3, Sigma-Aldrich, 99.99%) in an aqueous solution of nitric acid (HNO_3, LabSynth, 37.0%) under heating. After that, the pH values were adjusted by adding deionized water for each reactional medium, followed by their evaporation until reaching pH igual to 5.

Characterization

The structural behavior of the samples were characterized by XRD using a Rigaku diffractometer model DMax/2500 with graphite monochromatized Cu Kα radiation ($\lambda = 0.15405$ nm), and Rietveld refinements of the

XRD standards were performed using the general structure analysis (GSAS) program. Raman spectroscopy scattering measurements were performed using a Horiba Jobin Model iHR550 spectrometer with an argon laser (λ = 514.5 nm). The morphological aspects were evaluated by scanning electron microscopy (SEM) in a Carl Zeiss Supra 35-VP microscope operating at 10.00 kV. Transmission electron microscopy (TEM) and high-resolution TEM (HR-TEM) were performed using a FEI Tecnai G2F20 (The Netherlands) microscope operating at 200 kV. High-angle annular dark-field (HAADF) image and elemental mapping by energy-dispersive X-ray spectroscopy (EDS) were recorded in the scanning TEM (STEM) mode. The optical properties were investigated by absorption spectroscopy in the UV–Vis range, using a Varian model 5G spectrometer, programmed in diffuse reflectance mode. The photoluminescent behavior of these samples was examined through the krypton laser excitation (λ = 350.7 nm) at room temperature PL spectroscopy, where a Thermal Jarrel-Ash Monospec monochromator and a Hamatsu R446 photomultiplier were coupled to a compact acquisition system of an SR-530 lock-in. These materials were also studied using a Fluorolog Jobin–Yvon Fluorolog III spectrofluorometer, under excitation of a xenon lamp using the excitation wavelength of 394 nm. The emission data from the emission spectra were used to obtain CIE chromaticity diagrams using Spectra Lux software.

Results and discussion

X-ray diffraction (XRD) and Rietveld refinement

Identification of the crystalline phases of the β-Ag_2MoO_4 and the β-$Ag_{2-3x}Eu_xMoO_4$ ($x = 0.0$; 0.0025; 0.005; 0.0075, and 0.01 mmol) samples was performed by XRD patterns and the results are presented in Fig. 1a. The diffraction peaks are related to the cubic spinel structure (space group *Fd-3m*), with eight molecular formulas per unit cell ($Z = 8$), consistent with the results reported in the Inorganic Crystal Structure Database (ICSD) No. 238063 pattern (Galante et al. 2019). The absence of characteristic peaks of the precursors, such as Eu_2O_3 and Ag_2O, for instance, confirms that all the synthesized samples are perfectly monophasic. The narrow and well-defined profiles of the XRD peaks indicate the high crystallinity of the materials (Zhang et al. 2011).

Figure 1b shows the magnification of the region between 31.4° and 32.4° (principal peak) for all the samples of β-$Ag_{2-3x}Eu_xMoO_4$ ($x = 0.0$; 0.0025; 0.005; 0.0075, and 0.01 mmol). This figure shows that as the concentration of Eu^{3+} increases in the matrix a small displacement to lower values of 2θ for the doped samples in relation to the pure sample can be seen, which was noticed in a major degree for the sample containing 0.005 mmol of Eu^{3+}. This variation indicates the insertion of Eu^{3+} into the lattice of the β-Ag_2MoO_4, and a possible formation of oxygen and silver vacancies (relaxation of the crystalline lattice), and the different charge density of the silver and europium ions. The insertion of Eu^{3+} cation replacing Ag^+ cation forms two silver vacancies in the β-Ag_2MoO_4 matrix, and as the concentration of Eu^{3+} cations increases in the lattice, a higher concentration of silver vacancies will be formed. Thus, to observe the structural behavior of the β-Ag_2MoO_4 with the insertion of Eu^{3+} cations in the lattice, the Rietveld refinement was made. The results are presented in Table ESI.1 and Figure ESI.1 (a-e). The fitting parameters (R_{Bragg} and χ^2) indicate a good agreement between the XRD patterns calculated by this method and the experimental data observed for the as prepared β-Ag_2MoO_4 and β-$Ag_{2-3x}Eu_xMoO_4$ ($x = 0.0$; 0.0025; 0.005; 0.0075, and 0.01 mmol) microcrystals. Moreover, the lattice parameters (*a*, *b, c*) and bond angle (β), which were estimated from the refinement, confirmed the spinel cubic structure for all of the samples, and are also in good agreement with the ICSD No. 238063 card (Galante et al. 2019). When we compare the volume of the unit cell between the samples, we find that the volume of the doped samples decreased in relation to the volume of the sample cell. Thus, a possible replacement of silver atoms by europium ones results in a contraction of the unit cell by distorting the silver clusters. In addition, a decrease in the statistical fitting parameter values was observed in Table ESI.1 as the Eu^{3+} concentration increases, suggesting that the dopant insertion promotes an increase in the long-range ordering.

Through the Rietveld refinement data, a representation of the unit cell of the β-$Ag_{2-3x}Eu_xMoO_4$ ($x = 0.0$; 0.0025; 0.005; 0.0075, and 0.01 mmol) (Fig. 2) was made using the Visualization for Electronic and Structural Analysis (VESTA) program (version 3.3.9 for 64-bit version of Windows). In the β-Ag_2MoO_4 unit cell, the Mo atoms are coordinated by four oxygen atoms forming tetrahedral [MoO_4] clusters, and the Ag atoms are coordinated by six oxygen forming octahedral [AgO_6] clusters. In the β-$Ag_{2-3x}Eu_xMoO_4$ ($x = 0.0$; 0.0025; 0.005; 0.0075, and 0.01 mmol) structure, the Eu^{3+} ions are located at the octahedral sites of silver, forming [EuO_6] clusters, due to their electronic charge density and coordination number similar to that of silver atoms (Pinatti et al. 2015).

An order/disorder effect analysis on [AgO_6] clusters was performed by bond distance and bond angle measurements for all β-Ag_2MoO_4:Eu^{3+} samples, as shown in Table 1. The results indicate small distortions in Ag−O bond distance in the [AgO_6] cluster with the insertion of Eu^{3+} in the β-Ag_2MoO_4 matrix. The lengthening of the Ag−O bond is possibly related to the breakage of silver bond of [AgO_6] cluster and formation of new [EuO_x] clusters as a result of silver cluster distortions due to the possible formation of silver and oxygen vacancies in to the network. These distortions extend throughout the crystal lattice, which were

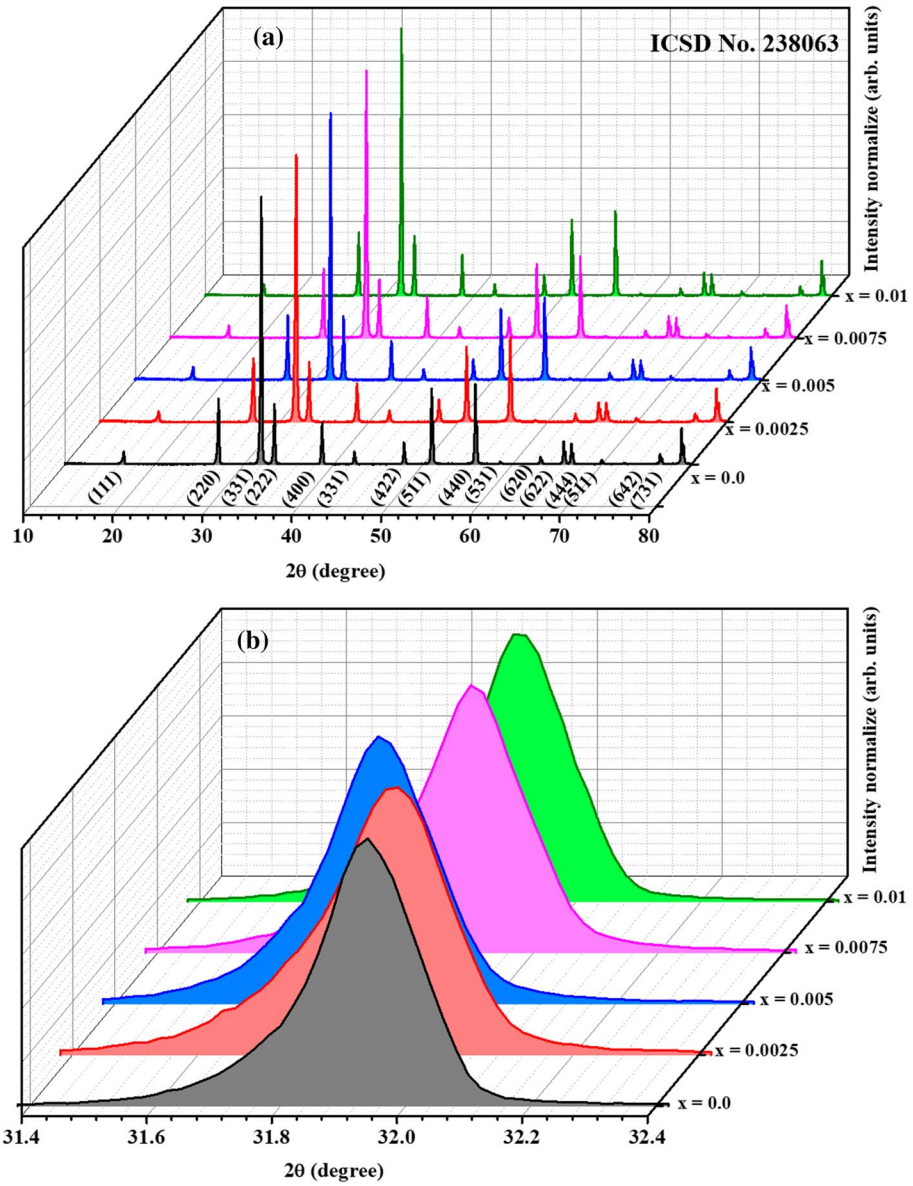

Fig. 1 **a** XRD patterns of β-$Ag_{2-3x}Eu_xMoO_4$ ($x = 0.0$; 0.0025; 0.005; 0.0075, and 0.01 mmol) powders synthesized by the co-precipitation method. **b** Magnification of the main peak (331)

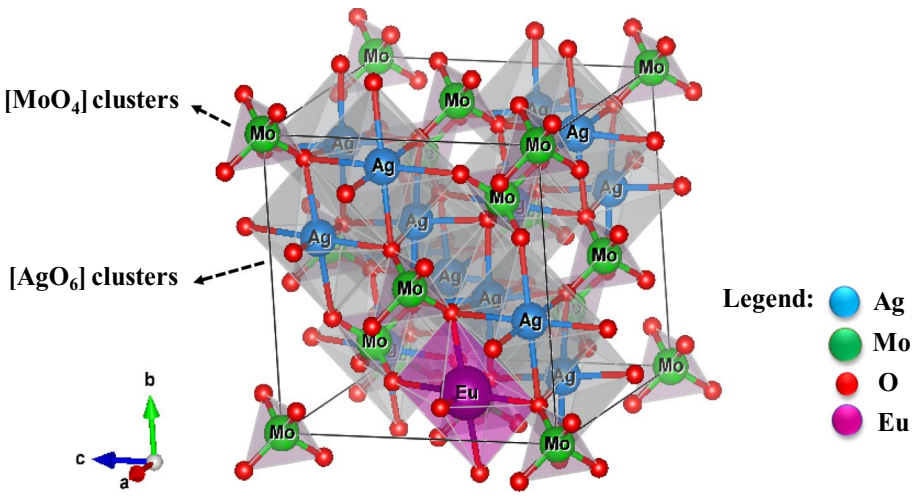

Fig. 2 Unit cell of cubic spinel structure of β-$Ag_{2-3x}Eu_xMoO_4$ ($x = 0.0$; 0.0025; 0.005; 0.0075, and 0.01 mmol)

Table 1 Ag−O bond distance and O−Ag−O bond angle of the octahedral [AgO_6] clusters of β-$Ag_{2-3x}Eu_xMoO_4$ ($x=0.0$; 0.0025; 0.005; 0.0075, and 0.01 mmol) unit cell

β-$Ag_{2-3x}Eu_xMoO_4$	Ag−O bond (Å)	O−Ag−O bond angle (°)
$x=0$	1.627(0)	109.47 (0)
$x=0.0025$	1.782 (4)	109.47 (15)
$x=0.005$	1.821 (0)	109.47 (0)
$x=0.0075$	1.771 (3)	109.47 (13)
$x=0.01$	1.768 (4)	109.47 (14)

ascribed to the Eu^{3+} doped samples having a higher long-range disorder.

Raman spectroscopy

In this study, Raman scattering spectroscopy was used to identify active vibrational modes and short-range structural order. The total irreducible representation of the vibrational modes for the β-Ag_2MoO_4 is shown at points in the Brillouin zone as described in Eq. 1:

$$(\Gamma\text{Raman}) + [\text{Infra - red}] = \left(A_{1g} + E_g + 3T_{2g} + T_{1g}\right) + \left[4T_{1u} + 2_{A2u} + 2E_u + 2T_{2u}\right] \quad (1)$$

where the modes A_{1g}, E_g and T_{2g} are active in the Raman, and the T_{1g} mode has a low intensity or is considered inactive. T_{1u} modes are detectable in IR spectra; the other modes $[2A_{1u}+2E_u+2T_{2u}]$ are inactive. The subscript terms "g″ and "u" indicate that the β-Ag_2MoO_4 presents an inversion center. Therefore, according to the group theory, the synthesized samples present a total of five active Raman modes (Fig. 3a), represented in Eq. 2:

$$\Gamma = A_{1g} + E_g + 3T_2 \quad (2)$$

The most intense peak at approximately 869 cm^{-1} corresponds to the active mode A_{1g}. This mode is related to the symmetrical stretching of the Mo–O bond, which occurs in the symmetric vibrations in the [MoO_4] clusters (Moura et al. 2016; Beltrán et al. 2014). T_{2g} mode was detected at around 274.85 cm^{-1} and refers to the asymmetric stretching of the Mo–O bond in the [MoO_4] clusters. The peak at 372 cm^{-1} is linked to the T_{2g} mode due to the asymmetric bending in the [MoO_4] clusters. The peak at about 273.82 cm^{-1} is associated with the E_g mode and occurs due to the vibrations of the external structure of the octahedral [AgO_6] clusters. The fifth peak, assigned to the T_{2g} mode, should appear in the region between 75 and 102 cm^{-1}, which is related to the mobility of O atoms in the structure (Moura et al. 2016; Kumar et al. 2016); this peak was not detected experimentally probably due to the low resolution of the equipment. The Raman modes for the agglomerates [AgO_6] were attributed to peaks located at 200 and 300 cm^{-1}. Figure 2b shows the magnification of the main peak located at around 869 cm^{-1} corresponding to the active mode A_{1g}. Analyzing this magnification (Fig. 2b) in relation to Fig. 2a, a small shifting of the baseline was observed for samples doped with Eu^{3+} and can be related to the distortions in the bond angles within the [MoO_4] clusters.

From the Raman spectra, it can also be observed that the synthesized powders are perfectly monophasic. There is no evidence of active modes related to impurity in the spectra of the samples analyzed. These results are in full agreement with the results obtained from the XRD standards. With the substitution of Ag^+ for Eu^{3+}, and the consequent formation of vacancies of Ag, the connection angles of the clusters were changed. These kind of disturbances cause changes in the symmetry, as well as in the periodicity of atoms result microcrystals of β-$Ag_{2-3x}Eu_xMoO_4$ with different degrees of ordering at short range distances.

Morphological analysis

The morphological analysis of the samples were conducted by SEM. Figure 4 shows the micrographs of the β-Ag_2MoO_4 and β-$Ag_{2-3x}Eu_xMoO_4$ ($x=0.0025$; 0.005; 0.0075; and 0.01 mmol) samples.

As shown in Fig. 4a, the sample of β-Ag_2MoO_4 shows an agglomerate of particles with no defined geometry, with an elongated shape and irregular distribution. The surface is smooth, with a well-defined grain, as seen in more detail in the isolated particles shown in Figure ESI-2a. The sample doped with 0.0025 mmol Eu^{3+} (Fig. 4b) the elongated shape is evident again, in this case, however, the particles have a certain roughness, with small structures randomly distributed on the surface (Figure ESI- 2b). In the sample containing 0.005 mmol of Eu^{3+}, shown in Fig. 4c and Figure ESI-2c, a change in the morphological profile of the particles can be observed. Apparently, the particles take on a wider shape with an irregular surface and small structures distributed over the entire surface, with a possible trend in geometric shapes similar to cubes. This new profile is highlighted with a lighter blue color and also in the isolated particles shown in Figure ESI-2c. This profile is also observed for samples with 0.0075 mmol Eu^{3+}, emphasizing the pink particles shown in Fig. 4d and with more details on the isolated particles in Figure ESI-2d.

The tendency to form cubes, observed in samples containing 0.005 and 0.0075 mmol of Eu^{3+}, is confirmed in Fig. 4e and Figure ESI-2e, where perfect cubes are easily identified (highlighted in light green) in the middle of the elongated

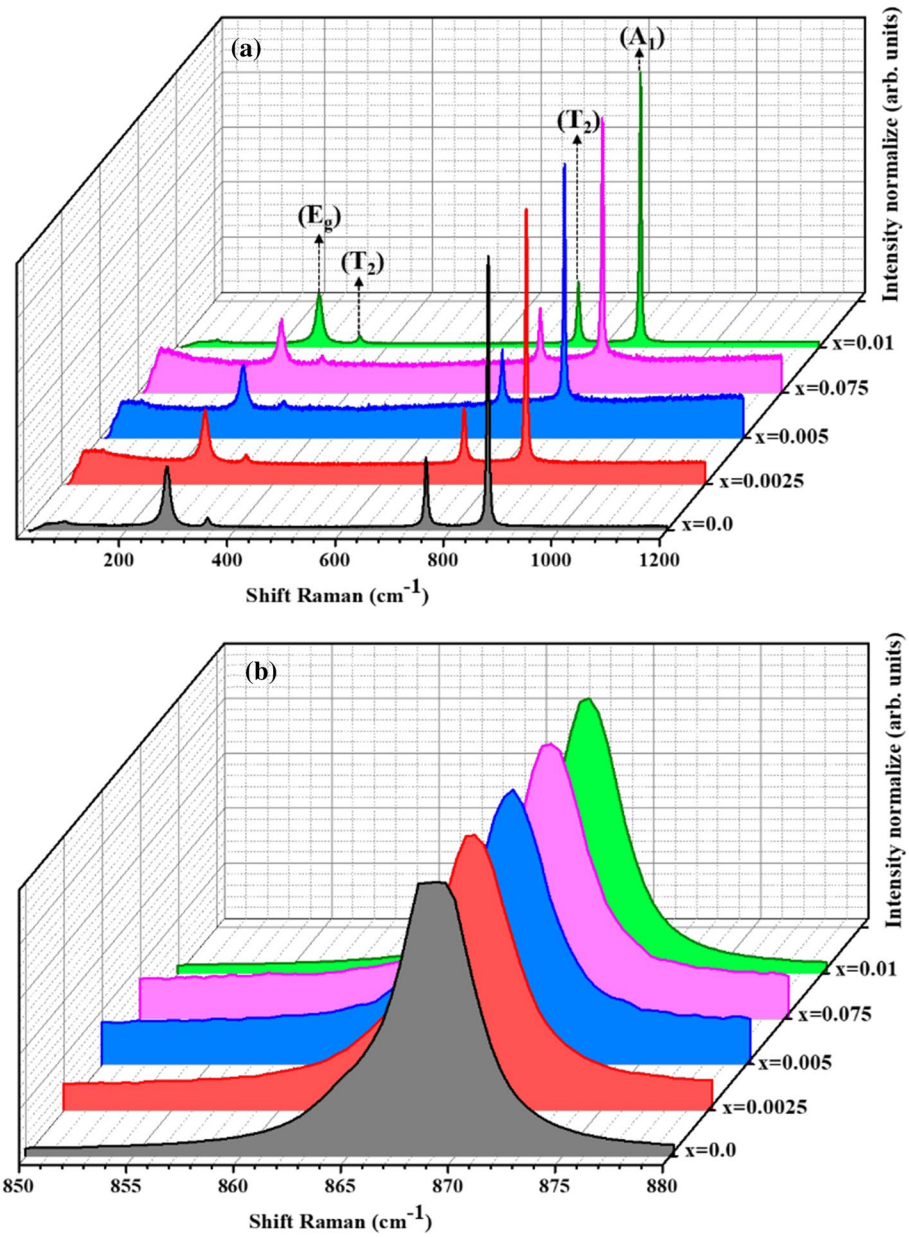

Fig. 3 **a** Raman spectra obtained for the β-$Ag_{2-3x}Eu_xMoO_4$ ($x = 0.0$; 0.0025; 0.005; 0.0075, and 0.01 mmol) samples. **b** Amplification of the main peak ascribed to the mode A_1

particles. These observations lead us to believe that the purposeful insertion of Eu^{3+} ions in the β-Ag_2MoO_4 matrix favors the formation of cubic particles, this fact may be associated with the surface energies of β-Ag_2MoO_4. In a study previously carried out by our group (Fabbro et al. 2015), the available morphologies of β-Ag_2MoO_4 were obtained to construct a complete map by the calculated values of the surface energy and the Wulff construction. From the analysis of this map, it is known that with the increase of the values of the surface energy for the (011) surface, the particles assume a geometric shape closer to a cubic morphology. In this case, it is believed that the substitution process of Ag^+ for Eu^{3+} results in an increase in the values of the surface energy for (011) surface that is proportional to its concentration, with concomitant transformation to morphology observed for β-$Ag_{2-3x}Eu_xMoO_4$ ($x = 0.0025$; $x = 0.005$; $x = 0.0075$ and $x = 0.01$) samples.

In the next step, a TEM characterization of β-$Ag_{2-3x}Eu_xMoO_4$ sample ($x = 0.01$ mmol) with the highest Eu^{3+} concentration in Ag_2MoO_4 crystalline lattice was performed to further obtain information regarding the morphological and compositional aspects. Figure 5a shows a HAADF image of a region containing microparticles with irregular shapes. An elementary analysis of this region by EDS mapping (Fig. 5b–e) reveals an homogeneous distribution of Ag, Eu, Mo, and O elements, without any sign of Eu segregation. When analyzing the elemental mapping of a cubic microparticle (Figure ESI-3), it was found that

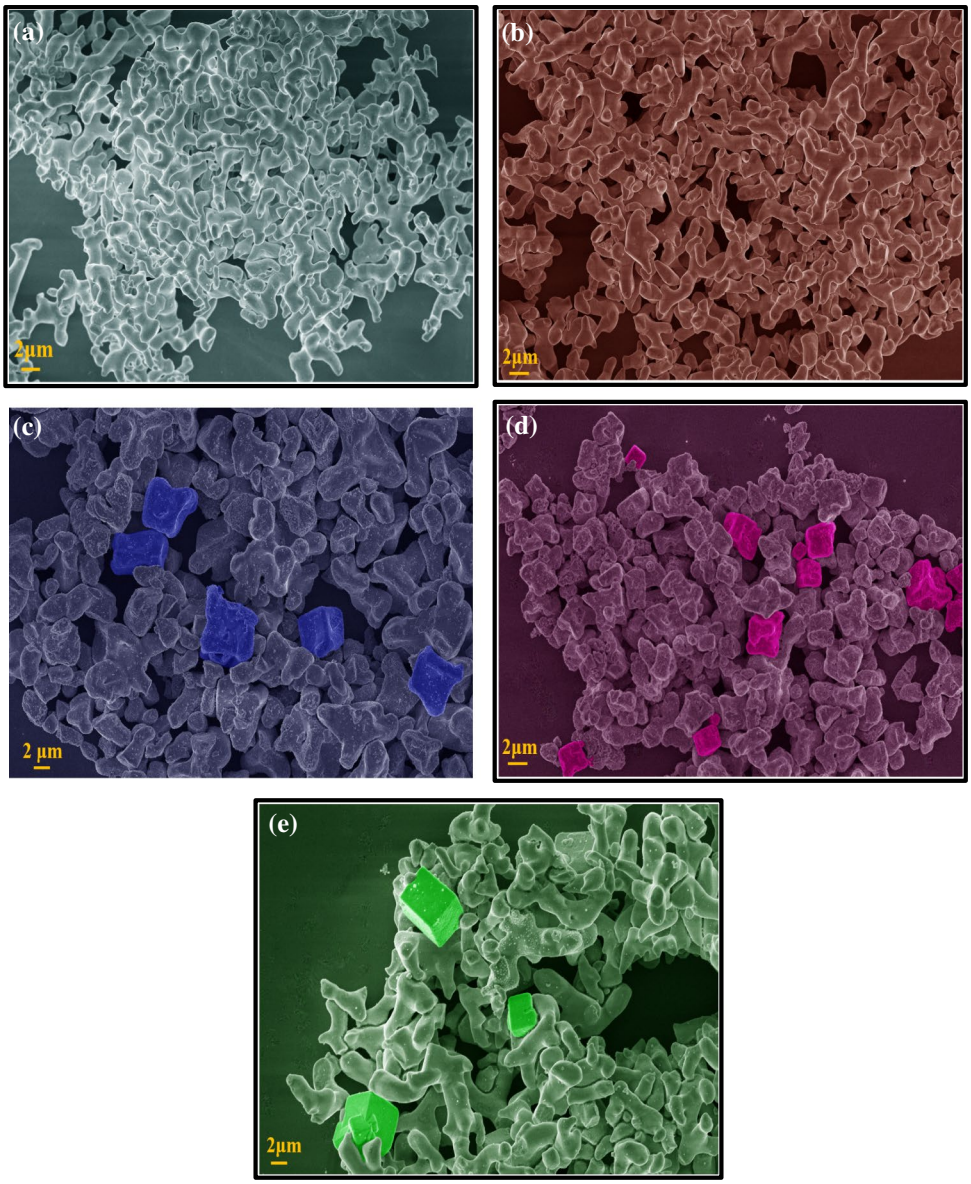

Fig. 4 SEM micrographs of the β-Ag_2MoO_4 and β-$Ag_{2-3x}Eu_xMoO_4$. **a** β-Ag_2MoO_4; **b** $x=0.0025$; **c** $x=0.005$; **d** $x=0.0075$; and **e** $x=0.01$

the distribution patterns of the analyzed elements are very similar to those observed in the microparticle shown in Fig. 5. Considering that the investigated microparticles were found in different regions, these results confirm that the Eu^{3+} dopant is well distributed into the β-Ag_2MoO_4:Eu^{3+} structure, reaffirming the efficiency of the preparation method.

Several NPs can be detected over the surface of β-$Ag_{2-3x}Eu_xMoO_4$ ($x=0.01$ mmol) microparticles, as can be seen in Fig. 5a. The EDS mapping indicates that only signals from the Ag element is present in these NPs (Fig. 5b) and could be associated to the growth of Ag^0 structures. This result is confirmed by the major Ag content observed by local EDS analysis of a single NP (Figure SI-4a–b). An estimation of the nanoparticle dimension gives an average size of 15 nm, as represented by the particle distribution graph (Figure SI-4c–d of SI file). Figure 5f shows a magnified view of a single NP, and Fig. 5g an HR-TEM image of a specific region, where the lattice fringes are sensed. The fast Fourier transform (FFT) of this region is illustrated in Fig. 5h, where an interplanar distance of 2.04 Å is observed, which is associated to the (200) family of planes of metallic Ag with a centered cubic (*fcc*) structure, in agreement with the ICSD database No. 604630 (Eric and Jette 1935).

The growth of metallic NPs over the surface of complex oxides is a well-known process which occurs because of their exposure to the electron beam irradiation of electronic microscopes (Gonzalez-Martinez et al. 2016). Specifically, Ag-based materials are prone to this mechanism, such as Ag_2WO_4, Ag_3PO_4, $AgVO_3$, and so on (Longo et al. 2013; Botelho et al. 2015; de Oliveira et al. 2016). As soon as the incident electrons interact with β-$Ag_{2-3x}Eu_xMoO_4$ ($x=0.01$ mmol) microcrystals, the reduction of [AgO_6]

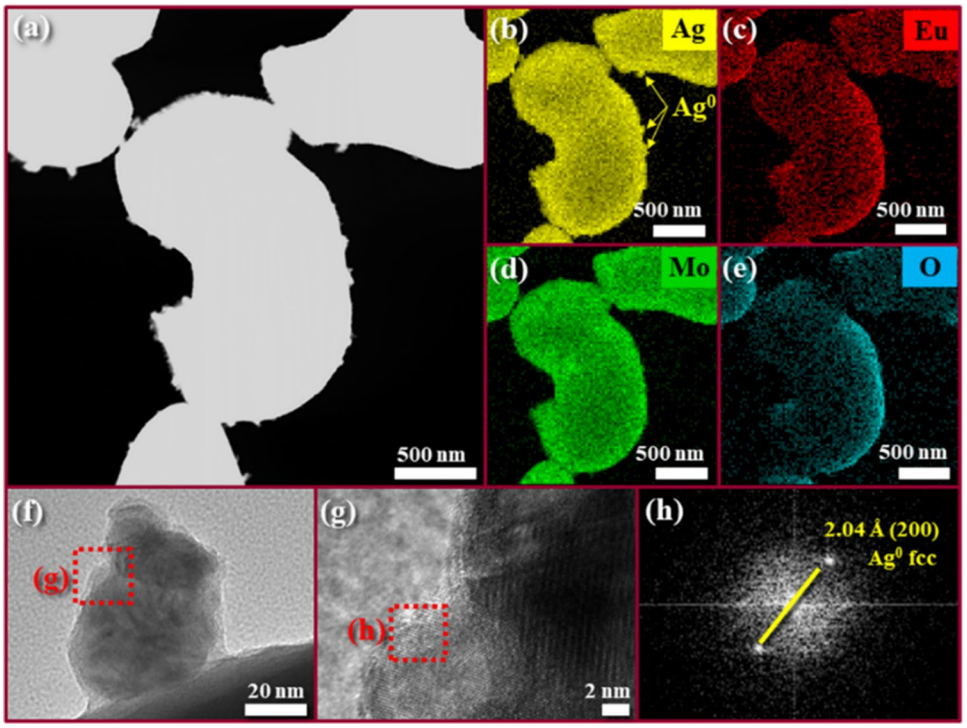

Fig. 5 TEM characterization of β-$Ag_{2-3x}Eu_xMoO_4$ sample ($x = 0.01$ mmol). **a** HAADF image of microcrystals with irregular shape, and **b**–**e** elemental distribution by EDS mapping for Ag, Eu, Mo, and O, respectively. **f** Magnified view of a grown NP, **g** HR-TEM image, and **h** FFT analysis showing evidence of the (200) plane of Ag^0

clusters to Ag^0 takes place. Subsequently, these Ag^0 species are extruded from the oxide structure and then the nucleation and growth processes of the Ag^0 NPs at around all irradiated regions are observed.

UV–Vis diffuse reflectance spectroscopy

The diffuse reflectance UV–Vis absorption spectra for the synthesized samples were analyzed according to the Kubelka–Munk and Wood-Tauc equation (Wood and Tauc 1972; Philips-Invernizzi 2001). According to previously published works, β-Ag_2MoO_4 microcrystals exhibit an optical absorption spectrum driven by indirect electronic transitions, the result of the return of electrons located in minimum energy states of the conduction band to the maximum energy states of the valence band in distinct points in the Brillouin area (Gouveia et al. 2014; Sousa et al. 2018). The electronic transitions and E_{gap} values obtained for the β-Ag_2MoO_4 and β-$Ag_{2-3x}Eu_xMoO_4$ ($x = 0.0025$; $x = 0.005$; $x = 0.0075$ and $x = 0.01$) samples are shown in Figure SI-5. The E_{gap} values of the β-$Ag_{2-3x}Eu_xMoO_4$ ($x = 0$; 0.0025; 0.005; 0.0075; and 0.01 mmol) samples were evaluated at around 3.5 eV in accordance with the literature data. In other studies performed by our group, the E_{gap} values calculated for pure β-Ag_2MoO_4 are in the range of 3.2 and 3.3 eV (Cunha et al. 2015; Montenegro et al. 2018).

Photoluminescent properties

Figure 6 shows the emission spectra recorded at room temperature of the β-$Ag_{2-3x}Eu_xMoO_4$ ($x = 0.0$, 0.0025, 0.005, 0.0075, and 0.01 mmol Eu^{3+}) samples excited by a 350.7 nm line of a krypton ion laser. By analyzing the emission spectra, it can be observed that all the synthesized samples present a broad band in the blue region, located between 350 and 550 nm with a maximum emission located at approximately 450 nm, characteristic of the β-Ag_2MoO_4 matrix (Figure ESI-6). This PL process involves the participation of several energy levels as a result of electronic transitions. It is believed that this behavior of β-Ag_2MoO_4 matrix is due to the different organizations of the energy levels within the band gap, which are caused by changes in the arrangement of the atomic arrangements present in the [MoO_4] tetrahedral and [AgO_6] octahedral clusters, where polarization occurs (Sczancoski et al. 2010; Gupta et al. 2015; Gouveia et al. 2014). According to the literature (Gouveia et al. 2014), the silver and oxygen vacancies, deformation bond angles, and surface defects play an important role in the visible emission. These distortions can change the lengths, as well as the angles in the Ag–O and Mo–O bonds, promoting alterations in the electronic properties of the material.

Moreover, besides the broad band in the blue region, Eu-doped samples present narrow well-defined lines characteristic of the Eu^{3+} ion in the 575–725 nm range. These

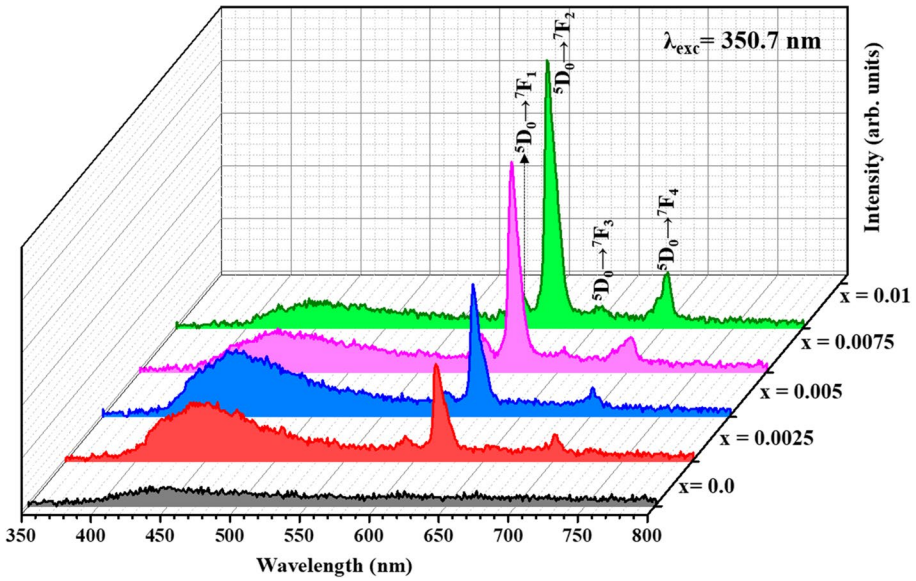

Fig. 6 β-$Ag_{2-3x}Eu_xMoO_4$ ($x=0.0$, 0.0025, 0.005, 0.0075, and 0.01 mmol Eu^{3+}) emission spectra at room temperature, $\lambda_{exc}=350.7$ nm of a Krypton ion laser

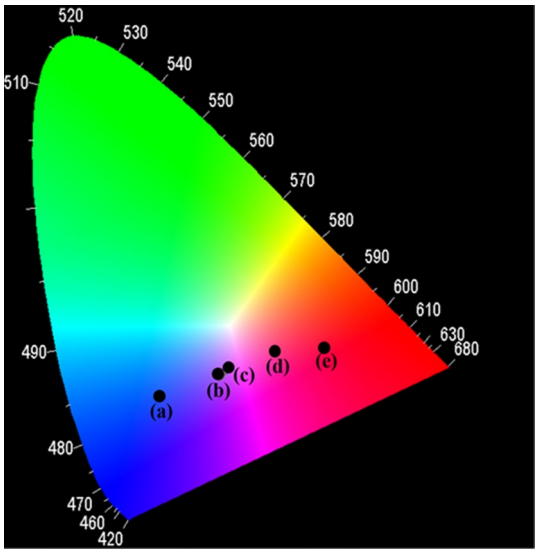

Fig. 7 CIE diagram coordinates of the β-$Ag_{2-3x}Eu_xMoO_4$, where **a** $x=0.0$, **b** $x=0.0025$, **c** $x=0.005$, **d** $x=0.0075$, and **e** $x=0.01$ (krypton laser, $\lambda=350.7$ nm)

lines are ascribed to the $^5D_0 \rightarrow {}^7F_J$ ($J=1$, 2, 3, and 4) transitions, and are observed at 593, 616, 653, and 701 nm, respectively. These results indicate that red phosphorus was obtained due to the greater efficiency in the energy transfer from the $[MoO_4]$ to the $[EuO_8]$ clusters. The appearance of these transitions confirms β-Ag_2MoO_4 as a good host for sensitizing the red emission of Eu^{3+}.

The PL emission data of the β-$Ag_{2-3x}Eu_xMoO_4$ (where $x=0.0$; 0.0025; 0.005; 0.0075, and 0.01 mmol of Eu^{3+}) samples were used to construct the chromaticity diagram as shown in Fig. 7, and 0.01 mmol of Eu^{3+}), represented by (a), (b), (c), (d), and (e), respectively. The calculated values for the X and Y coordinates of the synthesized samples are listed in Table 2 and symbolized in the chromaticity diagram by small black spheres.

Analyzing the data presented in Table 2, it can be observed that the Eu^{3+} insertion resulted in an increase in the y coordinate values for the Eu^{3+} doped β-Ag_2MoO_4 samples when compared to the pure one. The photoluminescence observed in these materials is associated both with the presence of shallow defect characteristic of more energetic regions (emission between violet and blue), as well as deep defects, which corresponds to less energetic regions such as the red range of the visible electromagnetic spectrum (Binnemans 2009). It can be inferred that by inserting Eu^{3+} into the β-Ag_2MoO_4 host, an efficient emission modeling can be obtained through the blue, violet, pink, and reddish orange ranges, indicating the use of these powders for different applications in the material science area.

Table 2 Values of the x and y coordinates of the chromaticity diagram of the powders of β-$Ag_{2-3x}Eu_xMoO_4$, where $x=0.0$; 0.0025; 0.005; 0.0075, and 0.01 mmol Eu^{3+}

Excitation source	Coordinates	$x=0.00$	$x=0.0025$	$x=0.005$	$x=0.0075$	$x=0.01$
Laser ($\lambda=350.7$ nm)	x	0.22	0.33	0.34	0.43	0.52
	y	0.21	0.24	0.26	0.29	0.30
Lamp ($\lambda=394$ nm)	x	0.55	0.58	0.59	0.58	0.59
	y	0.37	0.36	0.35	0.35	0.35

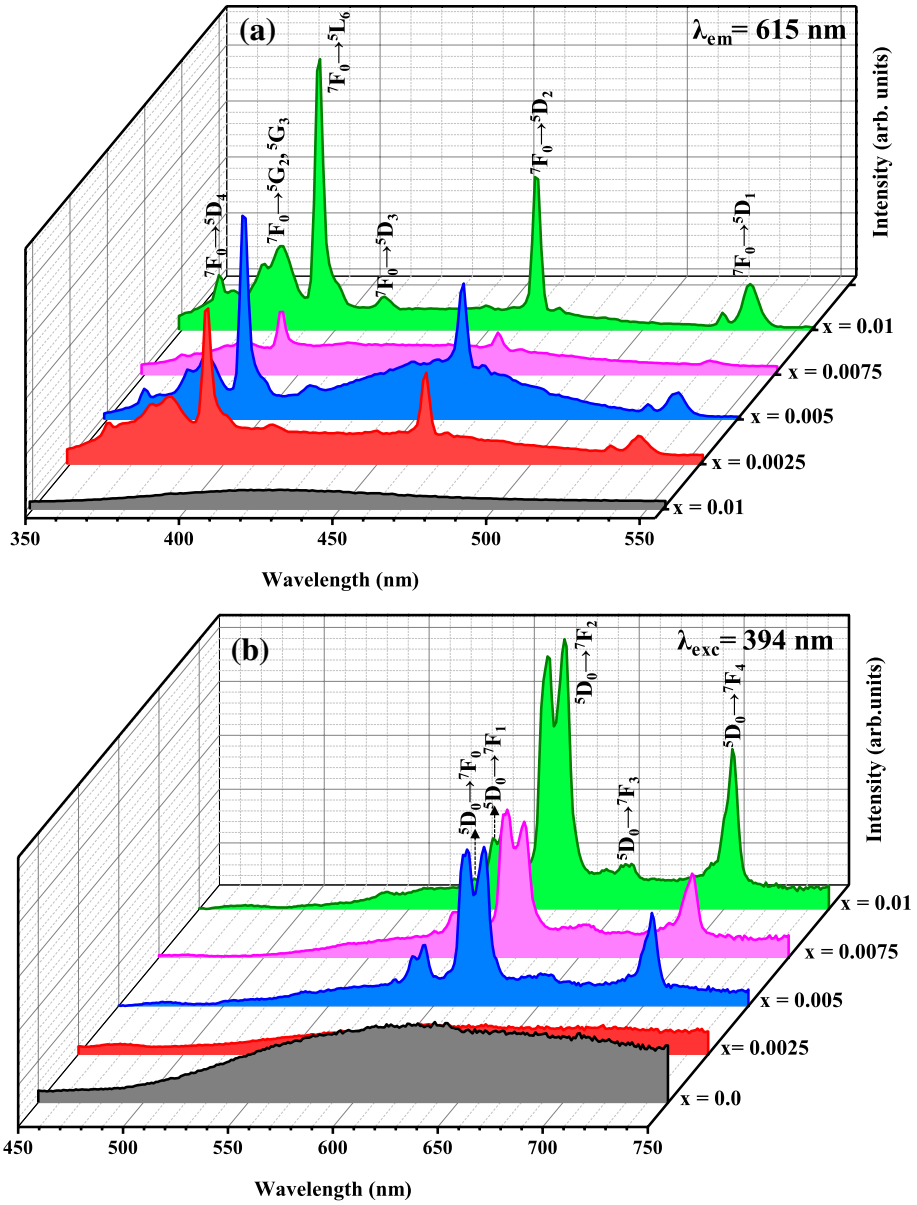

Fig. 8 **a** Photoluminescent excitation spectra of the samples β-$Ag_{2-3x}Eu_xMoO_4$ ($x = 0.0$; 0.0025, 0.005, 0.0075, and 0.01 mmol Eu^{3+}). $\lambda_{em} = 615$ nm. **b** Photoluminescent emission spectra of the samples β-$Ag_{2-3x}Eu_xMoO_4$ ($x = 0.0$; 0.0025, 0.005, 0.0075; and 0.01 mmol Eu^{3+}. $\lambda_{exc.} = 394$ nm at room temperature

The excitation spectra obtained by a xenon lamp (Fig. 8a) of the β-Ag_2MoO_4 and β-$Ag_{2-3x}Eu_xMoO_4$ (where $x = 0.0$; 0.0025; 0.005; 0.0075, and 0.01 mmol of Eu^{3+}) samples were obtained by setting the maxima emission wavelength at the emission of the Eu^{3+} ion located at 615 nm, which is ascribed to the $^5D_0 \rightarrow {}^7F_2$ transition.

Figure 8a shows that the most intense peak is located at 394 nm which corresponds to the $^7F_0 \rightarrow {}^5L_6$ transition, and at 465 nm which is ascribed to the $^7F_0 \rightarrow {}^5D_2$ transition. Peaks of lower intensities are located at 362 ($^7F_0 \rightarrow {}^5D_4$), 381 ($^7F_0 \rightarrow {}^5G_2$, $^5G_3$), 416 ($^7F_0 \rightarrow {}^5D_3$) and 535 nm ($^7F_0 \rightarrow {}^5D_1$) (Gupta et al. 2015). Figure 8b shows emission spectra for β-$Ag_{2-3x}Eu_xMoO_4$ ($x = 0.0$; 0.0025, 0.005, 0.0075, and 0.01 mmol Eu^{3+}) samples excited at 394 nm. Analyzing Figure ESI-7, it can be observed that the β-Ag_2MoO_4 broad band is suppressed by adding 0.0025 mmol Eu^{3+}. This effect is associated with the structural disorder of the clusters caused by doping. In higher Eu^{3+} concentrations, the formation of silver and oxygen vacancies cause matrix relaxation and the crystalline field is influenced, resulting in the characteristic transitions of the Eu^{3+} ions. The characteristic of these well-defined peaks are ascribed to the $4f \rightarrow 4f$ transitions of the Eu^{3+} ion, and are located at 580, 595, 618, 655, and 704 nm, related to the $^5D_0 \rightarrow {}^7F_J$ ($J = 1$, 2, 3, and 4) transitions, respectively (Fig. 8b) (de Oliveira et al. 2016). This ion is considered an excellent structural probe to investigate the chemical environment around it, mainly due to the $^5D_0 \rightarrow {}^7F_1$ (magnetic dipole) and $^5D_0 \rightarrow {}^7F_2$ (electric dipole)

transitions. The presence of $^5D_0 \rightarrow {}^7F_2$ transition is more intense than the $^5D_0 \rightarrow {}^7F_1$ one, indicating that Eu^{3+} ion is located in a site without inversion of symmetry. In addition, the area ratio of $^5D_0 \rightarrow {}^7F_2$ and $^5D_0 \rightarrow {}^7F_1$ transitions provides information about the local symmetry of Eu^{3+}ions. The relative area of $(^5D_0 \rightarrow {}^7F_2)/(^5D_0 \rightarrow {}^7F_1)$ transitions for all β-$Ag_{2-3x}Eu_xMoO_4$ samples were calculated and the values obtained are 7.34, 7.03, and 7.31 for $x = 0.005$, $x = 0.0075$, and $x = 0.01$, respectively. The sample $x = 0.0025$ was not considered, because it presented insufficient Eu^{3+} transitions intensities. These similar results are coherent, because there is only one silver site in the Ag_2MoO_4 host lattice for europium substitution, indicating that Eu^{3+} ions occupy these Ag^+ sites because of similar coordination number and electronic density.

The chromaticity diagram showed in Fig. 9 and Table 2 presents the values of the x and y coordinates for the emission (xenon lamp, $\lambda_{exc} = 394$ nm) data of the β-Ag_2MoO_4 and β-$Ag_{2-3x}Eu_xMoO_4$ ($x = 0.0$; 0.0025; 0.005; 0.005; 0.0075, and 0.01 mmol of Eu^{3+}), represented by black spheres identified as (a), (b), (c), (d) and (e), respectively.

These values are close to those published for the chromaticity coordinates of the international standards of the commercial phosphorus Y_2O_2S: Eu^{3+}, where $x = 0.64$ and $y = 0.34$ (Liao et al. 2012). The points referring to the X and Y chromaticity coordinates are positioned in the red region of the diagram and correspond to the $^5D_0 \rightarrow {}^7F_2$ transition of Eu^{3+} (Pereira et al. 2015).

Decay curves of the Eu-doped samples were obtained fixing the emission ($\lambda = 615$ nm) and excitation ($\lambda = 394$ nm)

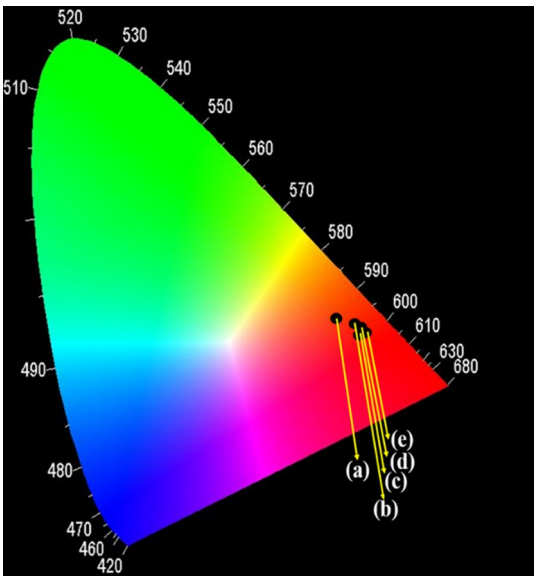

Fig. 9 Chromaticity diagrams of the β-$Ag_{2-3x}Eu_xMoO_4$, where **a** $x = 0.0$, **b** $x = 0.0025$, **c** $x = 0.005$, **d** $x = 0.0075$, and **e** $x = 0.01$ mmol samples

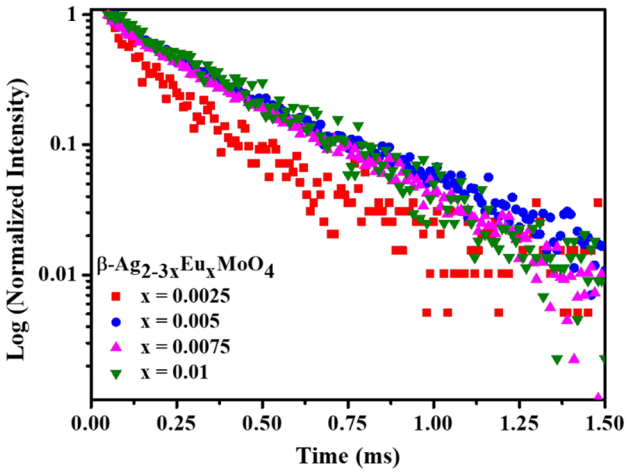

Fig. 10 Decay curves PL of the transition $^5D_0 \rightarrow {}^7F_2$ for Eu^{3+} in the β-$Ag_{2-3x}Eu_xMoO_4$ ($x = 0.00$; 0.0025, 0.005, 0.0075, and 0.01 mmol Eu^{3+}) samples

transitions of Eu^{3+}, and are shown in Fig. 10. The decay curves were well fitted through a first order exponential decay as shown in Eq. 3:

$$I(t) = I_0 \exp(-t/\tau), \tag{3}$$

where $I(t)$ is the intensity at the interval time t, I_0 is the initial intensity, and τ is the corresponding decay time. The profile of the curves indicates that one process governs the luminescence and this is a sign that the Eu^{3+} ions occupy only one kind of symmetry site in the β-$Ag_{2-3x}Eu_xMoO_4$ (**x** = 0.0; 0.0025; 0.005; 0.005; 0.0075, and 0.01 mmol of Eu^{3+}) host lattice. The $^5D_0 \rightarrow {}^7F_2$ decay times (τ) of the β-$Ag_{2-3x}Eu_xMoO_4$ were calculated as 0.145 for $x = 0.0025$; 0.266 for $x = 0.005$; 0.268 for $x = 0.0075$ and 0.290 ms for the $x = 0.01$ mmol samples, respectively.

Conclusions

We conclude that coprecipitation is a simple and efficient method of obtaining β-$Ag_{2-3x}Eu_xMoO_4$ ($x = 0.0$; 0.0025; 0.005; 0.005; 0.0075, and 0.01 mmol of Eu^{3+}) samples. The absence of secondary phases confirmed by XRD standards and Rietveld refinement indicates that doping was effective. The results of Raman spectroscopy corroborate to this observation, since no peaks additional to those predicted for the sample of β-Ag_2MoO_4 were detected. Therefore, we can say that the replacement of Ag^+ with Eu^{3+} ions caused a disturbance in the host of β-Ag_2MoO_4, which resulted in significant changes both in morphological and photoluminescence behavior. We observed that the variation in the concentration of the Eu^{3+} dopant favors the formation of particles with

defined geometric shape, especially cubes. When observing the isolated particles, it is noted in higher concentrations (0.01 mmol Eu^{3+}) perfect cubes, with well-defined edges and little roughness over the surface. On the other hand, with photoluminescence spectroscopy, using krypton laser (350.7 nm) and xenon lamp (394 nm) as excitation sources, we observed that by varying the concentration of Eu^{3+} inserted in the β-Ag_2MoO_4 matrix it is possible to modulate the intensity and the region, where the emission occurs. Pure β-Ag_2MoO_4 has a low intensity in the blue region, after the insertion of Eu^{3+} ions, this matrix changed their emission to the red region, with the intensity being directly related to the Eu^{3+} concentration. The modulation of the emission and morphology of these materials makes its potential for application in the areas of optoelectronics and catalysis.

Acknowledgements The authors are grateful for the support of São Paulo Research Foundation, FAPESP, (grant#13/07296-2, grant#13/23995-8, grant#16/05661-3, and grant#19/03722-3) and Prof. Maximo Si Liu, Prof. Andréa S. S. de Camargo Alvarez Bernardez and Tássia Gonçalvez from the physics institute of USP for the assistance with photoluminescence spectroscopy measurements.

Compliance with ethical standards

Conflict of interest The authors declare that they have no conflict of interest.

References

Beltrán A, Gracia L, Longo E, Andrés J (2014) First-principles study of pressure-induced phase transitions and electronic properties of Ag_2MoO_4. J Phys Chem C 118(7):3724–3732. https://doi.org/10.1021/jp4118024

Binnemans K (2009) Lanthanide-based luminescent hybrid materials. Chem Rev 109:4283–4374

Botelho G, Sczancoski JC, Andres J, Gracia L, Longo E (2015) Experimental and theoretical study on the structure, optical properties, and growth of metallic silver nanostructures in Ag_3PO_4. J Phys Chem C 119(11):6293–6306. https://doi.org/10.1021/jp512111v

Cichos J, Karbowiak M, Hreniak D, Stręk W (2016) Synthesis and characterization of monodisperse Eu^{3+} doped gadolinium oxysulfide nanocrystals. J Rare Earths 34(8):850–856. https://doi.org/10.1016/s1002-0721(16)60105-9

Cunha FS, Sczancoski JC, Nogueira IC, de Oliveira VG, Lustosa SMC, Longo E, Cavalcante LS (2015) Structural, morphological and optical investigation of β-Ag_2MoO_4 microcrystals obtained with different polar solvents. CrystEngComm 17(43):8207–8211. https://doi.org/10.1039/c5ce01662b

Dai P (2017) Enhanced red emission induced by Tb^{3+} doping in europium-based molybdate phosphors. Mater Res Bull 94:64–69. https://doi.org/10.1016/j.materresbull.2017.05.039

De Foggi CC, De Oliveira RC, Assis M, Fabbro MT, Mastelaro VR, Vergani CE, Gracia L, Andres J, Longo E, Machado AL (2020) Unveiling the role of beta-Ag_2MoO_4 microcrystals to the improvement of antibacterial activity. Mater Sci Eng 111:110765. https://doi.org/10.1016/j.msec.2020.110765

De Santana YVB, Gomes JEC, Matos L, Cruvinel GH, Perrin A, Perrin C, Andrès J, Varela JA, Longo E (2014) Silver molybdate and silver tungstate nanocomposites with enhanced photoluminescence. Nanomater Nanotechnol 4:22. https://doi.org/10.5772/58923

de Oliveira RC, Assis M, Teixeira MM, da Silva MDP, Li MS, Andres J, Gracia L, Longo E (2016) An experimental and computational study of β-$AgVO_3$: optical properties and formation of ag nanoparticles. J Phys Chem C 120(22):12254–12264. https://doi.org/10.1021/acs.jpcc.6b02840

Della Rocca DG, Victoria HFV, Moura-Nickel CD, Scaratti G, Krambrock K, De Noni A, Vilar VJP, Jose HJ, Moreira R (2020) Peroxidation and photo-peroxidation of pantoprazole in aqueous solution using silver molybdate as catalyst. Chemosphere 262:127671. https://doi.org/10.1016/j.chemosphere.2020.127671

Eric R, Jette FF (1935) Precision Determination of Lattice Constants. Journal of Chemical physics. https://doi.org/10.1063/1.1749562 10.1063/1.175193710.1063/1.33396510.1063/1.1749733

Erwin SC, Zu L, Haftel MI, Efros AL, Kennedy TA, Norris DJ (2005) Doping semiconductor nanocrystals. Nature 436(7047):91–94. https://doi.org/10.1038/nature03832

Fabbro MT, Saliby C, Rios LR, La Porta FA, Gracia L, Li MS, Andres J, Santos LP, Longo E (2015) Identifying and rationalizing the morphological, structural, and optical properties of β-Ag_2MoO_4 microcrystals, and the formation process of Ag nanoparticles on their surfaces: combining experimental data and first-principles calculations. Sci Technol Adv Mater 16(6):065002. https://doi.org/10.1088/1468-6996/16/6/065002

Fabbro MT, Foggi CC, Santos LP, Gracia L, Perrin A, Perrin C, Vergani CE, Machado AL, Andres J, Cordoncillo E, Longo E (2016) Synthesis, antifungal evaluation and optical properties of silver molybdate microcrystals in different solvents: a combined experimental and theoretical study. Dalton Trans 45(26):10736–10743. https://doi.org/10.1039/c6dt00343e

Ferreira EAC, Andrade Neto NF, Bomio MRD, Motta FV (2019) Influence of solution pH on forming silver molybdates obtained by sonochemical method and its application for methylene blue degradation. Ceram Int 45(9):11448–11456. https://doi.org/10.1016/j.ceramint.2019.03.012

Galante MT, Sotelo P, Hossain MK, Vali A, Raamann A, Longo C, Macaluso RT, Rajeshwar K (2019) Silver oxide-based semiconductors for solar fuels production and environmental remediation: a solid-state chemistry approach. ChemElectroChem 6(1):87–96. https://doi.org/10.1002/celc.201800885

Gonzalez-Martinez IG, Bachmatiuk A, Bezugly V, Kunstmann J, Gemming T, Liu Z, Cuniberti G, Rummeli MH (2016) Electron-beam induced synthesis of nanostructures: a review. Nanoscale 8(22):11340–11362. https://doi.org/10.1039/c6nr01941b

Guo W, Lin Y, Gong X, Chen Y, Luo Z, Huang Y (2008) Spectroscopic properties of Pr^{3+}:$KY(MoO_4)_2$ crystal as a visible laser gain medium. J Phys Chem Solids 69(1):8–15. https://doi.org/10.1016/j.jpcs.2007.07.085

Gouveia AF, Sczancoski JC, Ferrer MM, Lima AS, Santos MR, Li MS, Santos RS, Longo E, Cavalcante LS (2014) Experimental and theoretical investigations of electronic structure and photoluminescence properties of beta-Ag2MoO4 microcrystals. Inorg Chem 53(11):5589–5599. https://doi.org/10.1021/ic500335x

Gupta SK, Ghosh PS, Sudarshan K, Gupta R, Pujari PK, Kadam RM (2015) Multifunctional pure and $Eu^{(3+)}$ doped beta-Ag_2MoO_4: photoluminescence, energy transfer dynamics and defect induced properties. Dalton Trans 44(44):19097–19110. https://doi.org/10.1039/c5dt03113c

Jiang H, Liu J-K, Wang J-D, Lu Y, Yang X-H (2015) Thermal perturbation nucleation and growth of silver molybdate nanoclusters by a dynamic template route. CyrstEngComm 35:212–219

Kaddouri A, Tempesti E, Mazzocchia C (2004) Comparative study of β-nickel molybdate phase obtained by conventional precipitation and the sol-gel method. Mater Res Bull 39(4–5):695–706. https://doi.org/10.1016/j.materresbull.2003.11.005

Kianpour G, Soofivand F, Badiei M, Salavati-Niasari M, Hamadanian M (2016) Facile synthesis and characterization of nickel molybdate nanorods as an effective photocatalyst by co-precipitation method. J Mater Sci Mater Electron 27(10):10244–10251. https://doi.org/10.1007/s10854-016-5103-3

Krishna Bharat L, Lee SH, Yu JS (2014) Synthesis, structural and optical properties of $BaMoO_4$:Eu^{3+} shuttle like phosphors. Mater Res Bull 53:49–53. https://doi.org/10.1016/j.materresbull.2014.02.002

Kumar JV, Karthik R, Chen SM, Muthuraj V, Karuppiah C (2016) Fabrication of potato-like silver molybdate microstructures for photocatalytic degradation of chronic toxicity ciprofloxacin and highly selective electrochemical detection of H_2O_2. Scientific Rep 6:34149. https://doi.org/10.1038/srep34149

Laciste MT, de Luna MDG, Tolosa NC, Lu MC (2017) Degradation of gaseous formaldehyde via visible light photocatalysis using multi-element doped titania nanoparticles. Chemosphere 182:174–182. https://doi.org/10.1016/j.chemosphere.2017.05.022

Li S, Yu L, Sun J, Man X (2017) Synthesis and photoluminescent characteristics of Eu^{3+}-doped $MMoO_4$ (M=Sr, Ba) nanophosphors by a hydrothermal method. J Rare Earths 35(4):347–3355. https://doi.org/10.1016/s1002-0721(17)60918-9

Liao J, You H, Zhou D, Wen H-r, Hong R (2012) Sol–gel preparation and photoluminescence properties of $LiLa(MoO_4)_2$:Eu^{3+} phosphors. Opt Mater 34(8):1468–1472. https://doi.org/10.1016/j.optmat.2012.03.001

Lim CS (2016) Microwave sol–gel derived $NaCaGd(MoO_4)_3$:Er^{3+}/Yb^{3+} phosphors and their upconversion photoluminescence properties. Infrared Phys Technol 76:353–359. https://doi.org/10.1016/j.infrared.2016.02.012

Longo E, Cavalcante LS, Volanti DP, Gouveia AF, Longo VM, Varela JA, Orlandi MO, Andres J (2013) Direct in situ observation of the electron-driven synthesis of Ag filaments on alpha-Ag_2WO_4 crystals. Scientific Rep 3:1676. https://doi.org/10.1038/srep01676

Montenegro JE, Villalobos CM, Singh DP (2018) Ethylene glycol mediated facile and controlled growth of ultralong hexagonal silver molybdate microrods. Mater Lett 215:129–133. https://doi.org/10.1016/j.matlet.2017.12.068

Moura JVB, da Silva Filho JG, Freire PTC, Luz-Lima C, Pinheiro GS, Viana BC, Mendes Filho J, Souza-Filho AG, Saraiva GD (2016) Phonon properties of β-Ag_2MoO_4: Raman spectroscopy and ab initio calculations. Vib Spectrosc 86:97–102. https://doi.org/10.1016/j.vibspec.2016.06.009

Moura JV, Freitas TS, Cruz RP, Pereira RL, Silva AR, Santos AT, da Silva JH, Luz-Lima C, Freire PT, Coutinho HD (2017) beta-Ag_2MoO_4 microcrystals: characterization, antibacterial properties and modulation analysis of antibiotic activity. Biomed Pharmacother 86:242–247. https://doi.org/10.1016/j.biopha.2016.12.016

Ng CHB, Fan WY (2015) Uncovering metastable α-Ag2MoO4 phase under ambient condition. Overcoming high pressures by 2,3-Bis(2-pyridyl)pyrazine doping. Cryst Growth Des 15(6):3032–3037. https://doi.org/10.1021/acs.cgd.5b00455

Oliveira CA, Volanti DP, Nogueira AE, Zamperini CA, Vergani CE, Longo E (2017) Well-designed β-Ag_2MoO_4 crystals with photocatalytic and antibacterial activity. Mater Des 115:73–81. https://doi.org/10.1016/j.matdes.2016.11.032

Ouveia AF, Sczancoski JC, Ferrer MM, Lima AS, Santos MR, Li MS, Santos RS, Longo E, Cavalcante LS (2014) Experimental and theoretical investigations of electronic structure and photoluminescence properties of beta-Ag_2MoO_4 microcrystals. Inorg Chem 53(11):5589–5599. https://doi.org/10.1021/ic500335x

Pachauri N, Lakshmi G, Sri S, Gupta PK, Solanki PR (2020) Silver molybdate nanoparticles based immunosensor for the non-invasive detection of Interleukin-8 biomarker. Mater Sci Eng C 113:110911. https://doi.org/10.1016/j.msec.2020.110911

Pan Y, Zhang Q, Zhao C, Jiang Z (2007) Luminescent properties of novel Ho^{3+} and Tm^{3+} doped gadolinium molybdate nanocrystals synthesized by the Pechini method. Solid State Commun 142(1–2):24–27. https://doi.org/10.1016/j.ssc.2007.01.029

Pereira PFS, Nogueira IC, Longo E, Nassar EJ, Rosa ILV, Cavalcante LS (2015) Rietveld refinement and optical properties of $SrWO_4$:Eu^{3+} powders prepared by the non-hydrolytic sol-gel method. J Rare Earths 33(2):113–128. https://doi.org/10.1016/s1002-0721(14)60391-4

Philips-Invernizzi B (2001) Bibliographical review for reflectance of diffusing media. Opt Eng 40(6):1082. https://doi.org/10.1117/1.1370387

Pinatti IM, Nogueira IC, Pereira WS, Pereira PF, Goncalves RF, Varela JA, Longo E, Rosa IL (2015) Structural and photoluminescence properties of $Eu^{(3+)}$ doped alpha-Ag_2WO_4 synthesized by the green coprecipitation methodology. Dalton Trans 44(40):17673–17685. https://doi.org/10.1039/c5dt01997d

Sczancoski JC, Cavalcante LS, Marana NL, da Silva RO, Tranquilin RL, Joya MR, Pizani PS, Varela JA, Sambrano JR, Siu Li M, Longo E, Andrés J (2010) Electronic structure and optical properties of $BaMoO_4$ powders. Curr Appl Phys 10(2):614–624. https://doi.org/10.1016/j.cap.2009.08.006

Shahri Z, Sobhani A, Salavati-Niasari M (2013) Controllable synthesis and characterization of cadmium molybdate octahedral nanocrystals by coprecipitation method. Mater Res Bull 48(10):3901–3909. https://doi.org/10.1016/j.materresbull.2013.05.100

Singh DP, Sirota B, Talpatra S, Kohli P, Rebholz C, Aouadi SM (2012) Broom-like and flower-like heterostructures of silver molybdate through pH controlled self assembly. J Nanoparticle Res. https://doi.org/10.1007/s11051-012-0781-0

Sousa GdS, Nobre FX, Araújo Júnior EA, Sambrano JR, Albuquerque AdR, Bindá RdS, Couceiro PRdC, Brito WR, Cavalcante LS, Santos MRdMC, de Matos JME (2018) Hydrothermal synthesis, structural characterization and photocatalytic properties of β-Ag_2MoO_4 microcrystals: correlation between experimental and theoretical data. Arab J Chem. https://doi.org/10.1016/j.arabjc.2018.07.011

Sun W, Chen Z, Zhou J, Li D, Huang Z, Jin X, Zhang Q, Li F, Li Q (2016) Ytterbium-erbium ion doped strontium molybdate ($SrMoO_4$): synthesis, characterization, photophysical properties and application in solar cells. Phys Chem Chem Phys 18(48):33320–33328. https://doi.org/10.1039/c6cp06571f

Tang H, Lu A, Li L, Zhou W, Xie Z, Zhang L (2013) Highly antibacterial materials constructed from silver molybdate nanoparticles immobilized in chitin matrix. Chem Eng J 234:124–131. https://doi.org/10.1016/j.cej.2013.08.096

Tymiński A, Grzyb T (2017) Are rare earth phosphates suitable as hosts for upconversion luminescence? Studies on nanocrystalline REPO4 (RE=Y, La, Gd, Lu) doped with Yb^{3+} and Eu^{3+}, Tb^{3+}, Ho^{3+}, Er^{3+} or Tm^{3+} ions. J Lumin 181:411–420. https://doi.org/10.1016/j.jlumin.2016.09.028

Wang Z, Dai K, Liang C, Zhang J, Zhu G (2017) Facile synthesis of novel butterfly-like Ag_2MoO_4 nanosheets for visible-light driven photocatalysis. Mater Lett 196:373–376. https://doi.org/10.1016/j.matlet.2017.03.078

Wang L, Song Q, Guo X, Wang N, Wang X, Han Y, Xie J (2019) Synthesis of hollow spindle-like $CaMoO_4$:Ln^{3+}(Tb, Eu) phosphors for detection of iron(III) ions. Optik 185:957–964. https://doi.org/10.1016/j.ijleo.2019.04.044

Warmuth L, Ritschel C, Feldmann C (2020) Facet-, composition- and wavelength-dependent photocatalysis of Ag_2MoO_4. RSC Advances 10(31):18377–18383. https://doi.org/10.1039/d0ra02953j

Wood DL, Tauc J (1972) Weak absorption tails in amorphous semiconductors. Phys Rev B 5(8):3144–3151. https://doi.org/10.1103/PhysRevB.5.3144

Yang X, Wang Y, Xu X, Qu Y, Ding X, Chen H (2017) Surface plasmon resonance-induced visible-light photocatalytic performance of silver/silver molybdate composites. Chin J Catal 38(2):260–269. https://doi.org/10.1016/s1872-2067(16)62553-6

Zhang Y, Jiao H, Du Y (2011) Luminescent properties of HTP $AgGd_{1-x}W_2O_8:Eu_x^{3+}$ and $AgGd_{1-x}(W_{1-y}Mo_y)_2O_8:Eu_x^{3+}$ phosphor for white LED. J Lumin 131(5):861–865. https://doi.org/10.1016/j.jlumin.2010.12.002